metals

MDPI

Article

Structure Formation and Mechanical Properties of Wire Arc Additively Manufactured Al4043 (AlSi5) Components

Georgi Kotlarski [1,*], Maria Ormanova [1], Alexander Nikitin [2], Iuliia Morozova [2], Ralf Ossenbrink [2], Vesselin Michailov [2], Nikolay Doynov [2,3] and Stefan Valkov [1,4]

[1] Institute of Electronics, Bulgarian Academy of Sciences, Tzarigradsko Chaussee 72, 1784 Sofia, Bulgaria; maria.ormanova87@gmail.com (M.O.); stsvalkov@gmail.com (S.V.)
[2] Department of Joining and Welding Technology, Brandenburg University of Technology, Platz der Deutschen Einheit 1, 03046 Cottbus, Germany; alexander.nikitin@b-tu.de (A.N.); moroziul@gmail.com (I.M.); ralf.ossenbrink@b-tu.de (R.O.); fg-fuegetechnik@b-tu.de (V.M.); doynov@b-tu.de (N.D.)
[3] Institute of Metal Science, Equipment, and Technologies with Center for Hydro- and Aerodynamics, Bulgarian Academy of Sciences, 67 Shipchenski Prohod Blvd., 1574 Sofia, Bulgaria
[4] Department of Mathematics, Informatics and Natural Sciences, Technical University of Gabrovo, 4 Hadzhi Dimitar Str., 5300 Gabrovo, Bulgaria
* Correspondence: gvkotlarski@gmail.com

Abstract: In the current paper, the correlation between the physical size of additively built wire arc specimens and their structure and properties is studied. For the purpose of this work, two oval shaped specimens of different lengths were manufactured under the same technological conditions. The specimens have a length of 200 mm and 400 mm and will be referred to as L200 and L400. The microstructure of the samples was studied using X-ray diffraction analysis (XRD), optical microscopy, and scanning electron microscopy (SEM). The microhardness, yield strength (YS), and ultimate tensile strength (UTS) were determined and their correlation with the technological conditions of specimen build-up was clarified. The results of the carried out experiments indicated that the crystallographic structure of both specimens is similar. The scanning electron microscopy images show a higher concentration of irregularly shaped micro-pores formed near the edge of the αAl grains in the structure of the L400 specimen compared to the L200 one. An increase in the size of the αAl solid solution grains in the case of the L200 specimen towards its top section was noticed using optical microscopy. A slightly lower magnitude change was noticed concerning the L400 specimen. The increase in the size of the aluminum crystals was determined to be the increasing interpass temperature. Due to the much smaller thermal dissipation capacity of the smaller specimen, the interpass temperature of the same increased faster compared to the larger specimen. All of the above-mentioned factors led to a decrease in the microhardness of the specimens at higher stages of build-up. Since the specimens were deposited using similar layer deposition conditions, the resultant YS and UTS data are also highly comparable.

Keywords: structure; morphology; hardness; tensile strength; defects formation; WAAM; AlSi5; Al4043; GMAW; cold arc pulse

check for updates

Citation: Kotlarski, G.; Ormanova, M.; Nikitin, A.; Morozova, I.; Ossenbrink, R.; Michailov, V.; Doynov, N.; Valkov, S. Structure Formation and Mechanical Properties of Wire Arc Additively Manufactured Al4043 (AlSi5) Components. *Metals* **2024**, *14*, 183. https://doi.org/10.3390/met14020183

Received: 31 December 2023
Revised: 28 January 2024
Accepted: 31 January 2024
Published: 1 February 2024

Copyright: © 2024 by the authors. Licensee MDPI, Basel, Switzerland. This article is an open access article distributed under the terms and conditions of the Creative Commons Attribution (CC BY) license (https://creativecommons.org/licenses/by/4.0/).

1. Introduction

A very common method for the additive manufacturing of metallic components is based on direct energy deposition (DED) techniques. This incorporates additive manufacturing systems that use direct energy sources such as lasers, electron beams, and electric arcs to melt the used material and incorporate it into the general design of the output product [1]. A widespread DED technique is wire arc additive manufacturing (WAAM). The most commonly used setups for WAAM use an electric arc [2–4] and concentrated laser beams as heat sources [5–7]. The vastly different properties of the used heat sources determine their applicability in different research and industrial fields. Due to the high

energy density of the laser beam, much higher penetration into the welded material can be achieved while having much less thermal impact on the produced specimen due to a much lower thermal footprint [8]. For this reason, laser-based techniques are highly applicable for the manufacturing of small components with complicated shapes that require high precision of the manufacturing process [9]. In comparison, wire arc additive manufacturing techniques are predominantly based on using an electric arc as a heat source. Due to the much lower energy density of the electric arc, a much shallower, but wider weld seam is formed. Due to the larger footprint of the electric arc, the thermal impact on the specimens increases significantly [10,11]. These specifics of the WAAM method for component manufacturing determine its applicability for the manufacturing of large components where precision can be slightly compromised in favor of high deposition rates [12]. So far, different setups for wire arc additive manufacturing have been proposed with the most popular ones being gas metal arc welding (GMAW) and gas tungsten arc welding (GTAW) [13]. Both of these welding techniques have a high deposition rate, somewhat simple construction, and are highly compatible with the automatization process. The main difference between the two techniques is the way the filler material is fed through to the components. GMAW used a direct feed method where the filler material represents one of the electrodes and when applied to the substrates an arc between the substrates and the filler wire is formed. GTAW, on the other hand, uses a separate electrode made out of tungsten due to its high melting temperature and high thermal stability. The arc is formed between the tungsten electrode and the substrate, and the filler wire is fed into the formed plasma cavity. Gas metal arc welding itself divides into two main modes that are used to carry out the welding process—cold metal transfer (CMT) [14,15] and cold arc pulse [16]—although other work modes have been proposed [16]. The two modes are almost identical with the exception of the way the molten material is introduced into the structure of the manufactured component. During the CMT method, the separation of the molten material is carried out mechanically by moving the electrode wire forwards and backwards, while in the case of cold arc pulse method, the separation is carried out electronically using high-frequency switching.

The possibility of manufacturing large light metal components employing both methods is of utmost importance due to their widespread application in industrial, commercial, and research applications [17,18]. Aluminum and its alloys are some of the most sought after materials due to their excellent corrosion resistance, excellent mechanical properties, lightweight structure, and of course due to their very low cost. The Al4043 (AlSi5) hypoeutectic alloy is one of the most commonly studied aluminum alloys used in practice. This is attributed to its high weldability and corrosion resistance. The most commonly used WAAM method for the fabrication of Al4043 components is the CMT mode. Different strategies for the deposition of such components are discussed in the literature such as varying the path of the welding torch during the welding process [19]. Chuanchu et al. [19] have found that by varying the deposition path, it is possible to cause a deliberate change in the preferred crystallographic orientation of the specimens. This could also be achieved by changing the angle of the welding torch as Chakkravarthy et al. [20] have found. They describe that implementing a 10° angle of the welding torch leads to the manufacturing of a specimen with a preferred orientation of the unit cells towards the (111) crystallographic plane. Changing the angle of the torch to 15° causes a reorientation towards the (101) plane. Manufacturing specimens with a preferred crystallographic orientation towards the (111) plane signifies that a very low heat input was achieved. Another method for reducing the heat input during the welding process is the implementation of high-frequency pulses, otherwise known as pulsed cold metal transfer (CMT+P). Zhi-qiang et al. [21] have studied the influence of heat input on the geometrical shape, size, microstructure, and mechanical properties of the formed specimens by varying the wire feeding rate and the welding speed. They have found that the optimal wire feeding rate for producing Al4043 specimens using CMT+P is 66.7 mm/s, and the optimal welding speed is 8 mm/s. These results are confirmed by Pramod et al. [22] who have also used similar WAAM technological

conditions during their research. Employing such technological conditions leads to the manufacturing of specimens with the least amount of microstructural defects, which leads to an improvement in the mechanical properties of the specimens. Furthermore, Vishnukumar et al. [23] have found a correlation between the implementation of pulses during the welding process and the formation of differently structured αAl+Si eutectic structures. Using the CMT+P mode results in the formation of dense fibrous eutectics that improve the mechanical properties of the specimen. This was also confirmed by previous research [24]. In addition to this, the corrosion resistance of the manufactured components also increases, which is of high importance for the aircraft and shipbuilding industries.

Despite an abundant number of studies being present regarding the specifics of manufacturing Al4043 and similar hypoeutectic alloys, there is not enough research that describes the correlation between the physical size of manufactured components and their microstructure and mechanical properties. The physical size of WAAM components is an important factor from a practical point of view and also from a purely scientific interest. Changing the size of the components is a realistic situation that can occur during the designing and manufacturing stages due to optimization of the overall structure they will be incorporated in. Of course, a change in the size of the build details is undoubtedly going to result in a change in their microstructure and mechanical properties. The question at hand concerns the magnitude of this change and also how well the manufactured components would retain their mechanical strength as a function of their volume. This also validates the importance and accuracy of small-scale experiments such as the ones previously described. From a scientific point of view, it is interesting to observe the change in the properties of the specimens as a function of their volume and to determine the root cause of this phenomena. Additionally, most of the present research implements the manufacturing of components using the CMT+P mode, and there is very little (almost none) research regarding the application of the cold arc pulse mode for the manufacturing of light metal components.

Therefore, the goal of this work is to observe the effect of the physical size of Al4043 wire arc additively manufactured specimens, using GMAW in the cold arc pulse mode, on their resultant microstructure and mechanical properties. A special emphasis is paid to the significance of the results for determining the relevance of small-scale experiments and also determining the volumetric effect on the resultant properties of the examined specimens.

2. Experimental Setup

The setup used for the manufacturing of the currently studied specimens is shown in Figure 1. It consists of a robotic arm KUKA KR 15/1 (KUKA GmbH, Augsburg, Germany) combined with a MTR500W PP welding torch (EWM GmbH, Mündersbach, Germany) and a standard four roller type wire feeding unit (EWM GmbH, Mündersbach, Germany). The power supply used in the setup is the EWM Alpha Q 552 pulse MM RC power supply (EWM GmbH, Mündersbach, Germany) suitable for GMAW in the cold arc pulse mode. The specimens are built on a substrate made of Al 6082 T6 with dimensions of 300 × 65 × 15 mm. The substrate is mechanically cleaned with an abrasive paper followed by subsequent sterilization of the surface using 99% isopropyl alcohol. The substrate is placed on a water-cooled block designed to improve the cooling of the specimens during the manufacturing process. During the welding process, a large quantity of aluminum vapors are formed. As it is known, Al is highly toxic for living organisms so an appropriately selected ventilation system must be employed to extract the formed aluminum vapors during the process.

For the purpose of this research, two AlSi5 (Al4043) oval specimens were manufactured to a length of 200 mm (L200) and 400 mm (L400) using a welding wire with a diameter of 1.2 mm. A double increase in the size of the side wall of the specimens leads to an almost double increase in the surface area and volume of the specimens. This increase should be sufficient enough to achieve the goals of the present research. The chemical compositions of the AlSi5 wire and the substrate are presented in Table 1.

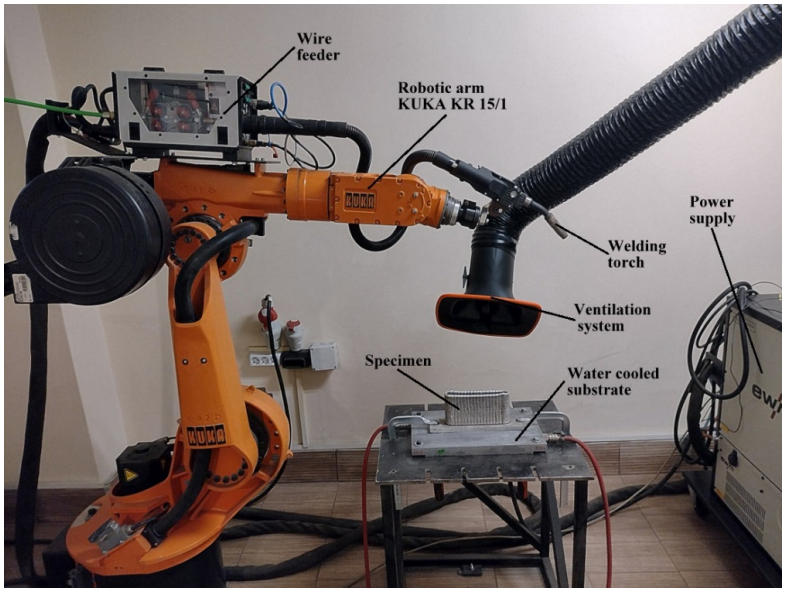

Figure 1. Wire arc additive manufacturing experimental setup.

Table 1. Chemical compositions of the substrate and the welding wire in wt%.

Alloy	Al	Si	Fe	Cu	Mn	Mg	Zn	Be	Ti	Cr	Others
AlSi5 (Al4043) (wire)	Bal.	4.5–5.5	0.6	0.3	0.15	0.2	0.1	0.0003	0.15	-	0.15
Al6062-T6 (substrate)	Bal.	1.2	0.5	0.1	0.4	0.6	0.2	-	0.1	0.25	0.15

The technological conditions of layer deposition are presented in Table 2. Both specimens were built using a welding speed of 12 mm/s. The formed components are shown in Figures 2a and 3a, respectively. The specimens are built up to a height of 140 mm. To exclude the effect of the wire feeding speed on the geometry and microstructure of the specimens, a constant wire feeding speed of 100 mm/s was used in all cases. The constant flow of protective Ar gas with a 99.999% purity was set to 17 L/min. The wait time in the case of the larger specimen was set to 30 s. Initially, the same wait time was applied for the smaller specimen; however, it proved to be insufficient due to the much smaller volume of the specimen and thus the much lower heat capacity. The very short time between subsequent layer deposition resulted in the formation of slag atop the surface of the specimen. This resulted in a rapid increase in the defects of the specimen due to the reduced fusion of the material. This necessitated the build-up of a new specimen with a higher wait time of 60 s. The highest detected layer temperature in the case of the L200 specimen right after the completion of the deposition process was 191 °C, which is comparable to the one reached while manufacturing the L400 specimen—189 °C. All measured values were obtained using an infrared thermometer KIRAY 300 (Kimo Instruments, Mumbai, India) capable of measuring surface temperatures in the range of −50 to +1850 °C. The offset in the direction of build-up in both cases was set to 1 mm. Samples of the bottom, middle, and top sections of each specimen were prepared in order to study the evolution of their structure as a function of the height.

Table 2. Technological conditions of specimen manufacturing.

Specimen	Voltage, V	Current, A	Gas Flow, L/min	V_{wire}, mm/s	$V_{welding}$, mm/s	Wait Time, s	Offset, mm
L200	17.5	90	17	100	12	60	1
L400	17.5	90	17	100	12	30	1

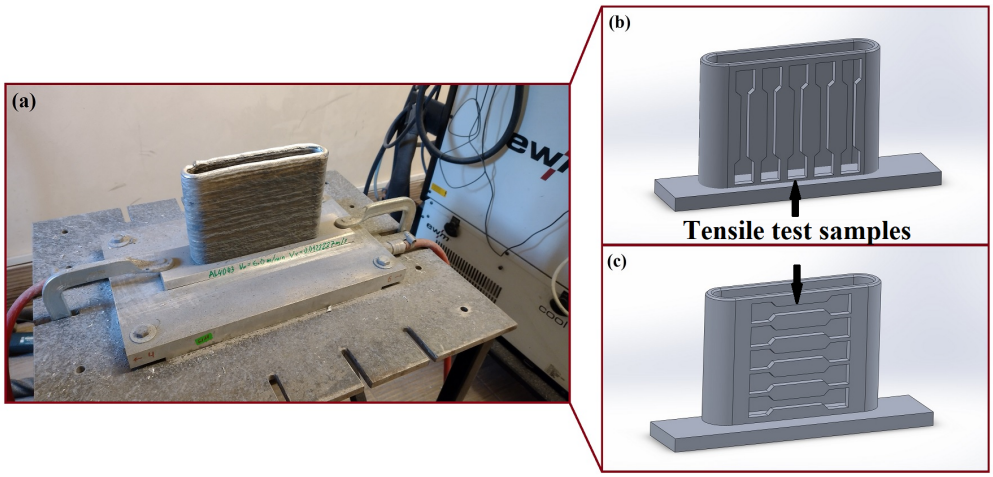

Figure 2. WAAM specimen with a length of 200 mm (**a**); vertical tensile test samples location (**b**); and horizontal tensile test samples location (**c**).

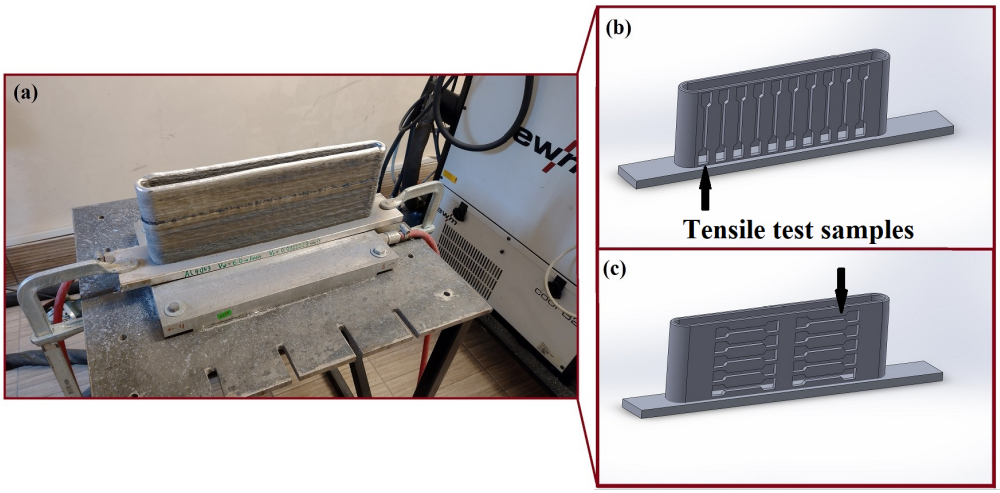

Figure 3. WAAM specimen with a length of 400 mm (**a**); vertical tensile test samples location (**b**); and horizontal tensile test samples location (**c**).

An X-ray diffraction analysis was performed in order to study the phase composition of the samples. The analysis was performed using the 2θ scale in the symmetrical Bragg–Brentano mode in the range of 30–80°. The wavelength of the used CuKα radiation was 1.54 Å. All the detected diffraction maxima were discerned using the ICDD (International center for diffraction data) crystallographic database PDF #040787 and PDF #271402, corresponding to the Al and Si phases.

Optical images of the specimens were taken using an optical microscope Drawell MIT 300/500 (Drawell, Chongqing, China) series microscope. Furthermore, the microstructure of the samples was studied in detail using scanning electron microscopy (SEM) (Tescan, Brno, Czech Republic) using a 20 kV high voltage source, and the chemical composition was determined using an energy dispersive X-ray spectroscopy (EDX) (Tescan, Czech Republic).

A ZwickRoell Dura Scan 10/20 G5 (ZwickRoell, Ulm, Germany) hardness tester in the Vickers hardness mode was employed for the determination of the hardness of all samples at the different stages of build-up. Ten consecutive experiments were carried out at a standard room temperature of 20 °C, at 50% humidity level, following the ISO 6507-1 standard [25]. The applied loading force was 1N in all cases.

The yield strength (YS), the ultimate tensile strength (UTS), and the elongation (ε) of the specimens were determined by performing tensile tests using a ZwickRoell Vibrophore 100 testing system (ZwickRoell, Ulm, Germany) in a static strain mode. During the tests,

samples from both the vertical and horizontal directions of build-up were examined. Figures 2b and 3b show the location of the vertical samples taken from both specimens, and Figures 2c and 3c show the location of the horizontal samples along the surface area of the manufactured components. The tensile strength probes all have a length of 130 mm, a thickness of 5 mm, and a shaft width of 10 mm. The experiments were performed in agreement with the DIN EN ISO 6892-1 standard [26].

3. Results

The X-ray diffraction analysis results regarding the bottom, middle, and top samples of both specimens are shown in Figure 4, where Figure 4a corresponds to the L200 specimen, and Figure 4b corresponds to the L400 one. The experimentally obtained diffractograms do not present amorphous-like halos confirming the crystalline structure of the built-up specimens. A double-phase structure consisting of aluminum and silicon phases was observed. This type of configuration is typical for eutectic alloys such as AlSi5 [27]. Aluminum and silicon both have a face-centered cubic (fcc) structure and belong to the Fm3m (225), and the Fd3m (227) space groups, accordingly. Diffraction maxima of the aluminum phase corresponding to the (111), (200), (220), and (311) planes, belonging to {111}, {100}, {110}, and {311} families of crystallographic planes, respectively, were observed. Peaks corresponding to the (220), (311), (400), and (331) planes of the Si phase were also detected.

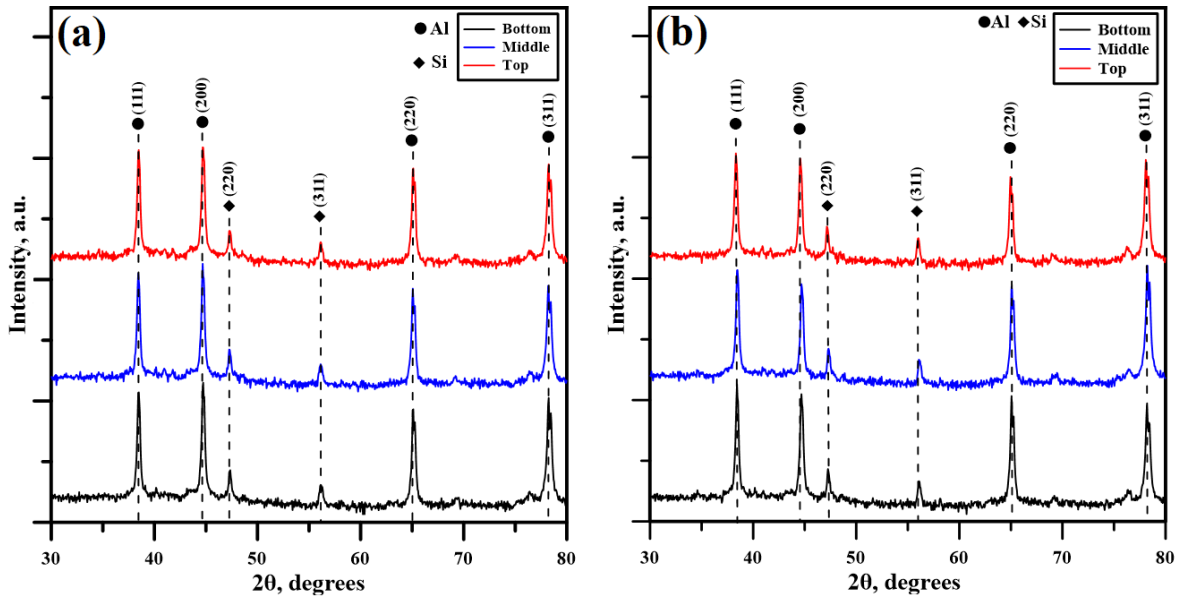

Figure 4. X-ray diffraction patterns of the top, middle, and bottom sections of the (**a**) L200 specimen and (**b**) L400 specimen.

In order to further evaluate the effect of the geometrical size on the crystallographic imperfections (such as dislocations, stacking faults, nanopores, etc.) of the specimens on the resulting structure, the full width at half maximum (FWHM) was determined using a specialized peak fitting software SciDAVis version 2.7. According to the theory of X-ray diffraction, the quantity of the crystallographic imperfections is proportional to the peak broadening, i.e., a higher value of FWHM corresponds to a greater amount of crystallographic imperfections [28]. Figure 5 presents a graphical comparison between the raw data and the resulting peak fit. As an illustration of the accuracy of the fitting model, an aluminum peak was chosen from the data, corresponding to the bottom of the L400 specimen. The shown fit indicates that the FWHM of that particular aluminum peak is 1.108 ± 0.035.

The remaining FWHM values with their respective margin of error are summarized and presented in Table 3.

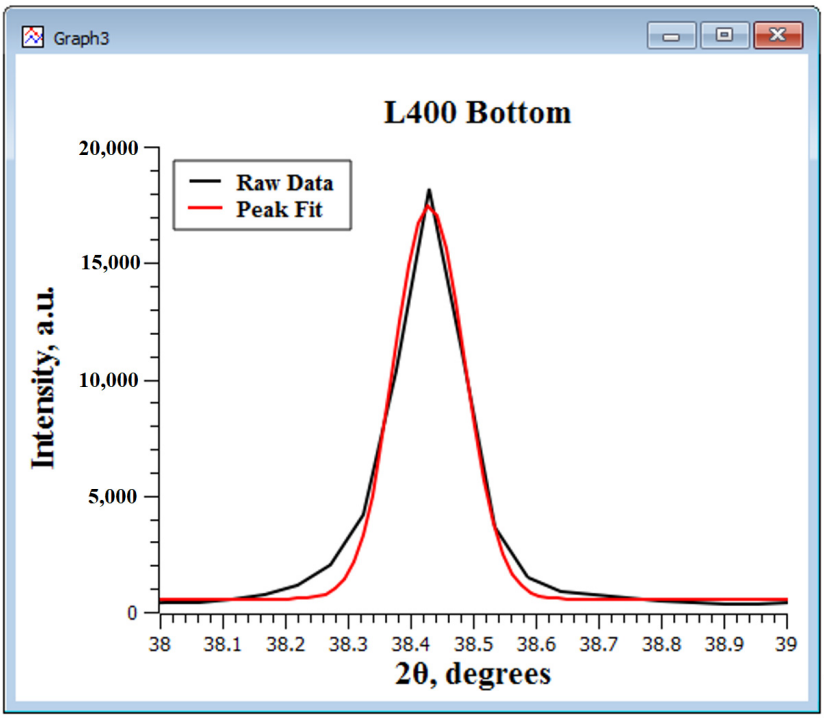

Figure 5. Graphical comparison between the raw data and the fitted peak.

Table 3. FWHM of the L200 and the L400 specimens at every stage of build-up.

Material and Detected Family of Planes	FWHM		
	L200 Specimen		
	Bottom	Middle	Top
Al {111}	1.278 ± 0.035	1.386 ± 0.044	1.594 ± 0.030
Al {100}	1.231 ± 0.062	1.202 ± 0.051	1.224 ± 0.031
Al {110}	1.119 ± 0.028	1.117 ± 0.033	1.218 ± 0.045
Al {311}	1.323 ± 0.045	1.345 ± 0.065	1.352 ± 0.054
	L400 specimen		
Al {111}	1.108 ± 0.035	1.518 ± 0.042	1.347 ± 0.051
Al {100}	1.202 ± 0.040	1.373 ± 0.049	1.479 ± 0.036
Al {110}	1.104 ± 0.067	1.157 ± 0.033	1.513 ± 0.064
Al {311}	1.459 ± 0.069	1.209 ± 0.052	1.321 ± 0.039

The results for the FWHM of the specimens, corresponding to the {111}, {100}, {110}, and {311} families of crystallographic planes, are presented in Figure 6a,b. The results indicate that there is no significant difference between the FWHM of the detected diffraction maxima at the different stages of build-up, and also between the values of the different specimens. This means that a similar concentration of the crystal lattice imperfections is to be expected.

In order to gain more knowledge of the change in the structure of the specimens during the manufacturing process, the interplanar spacing d (Å) and the lattice constant a (Å) of both primary materials comprising the AlSi5 alloy—Al and Si—were calculated. All calculations were performed using the equations presented in detail in the following work [29].

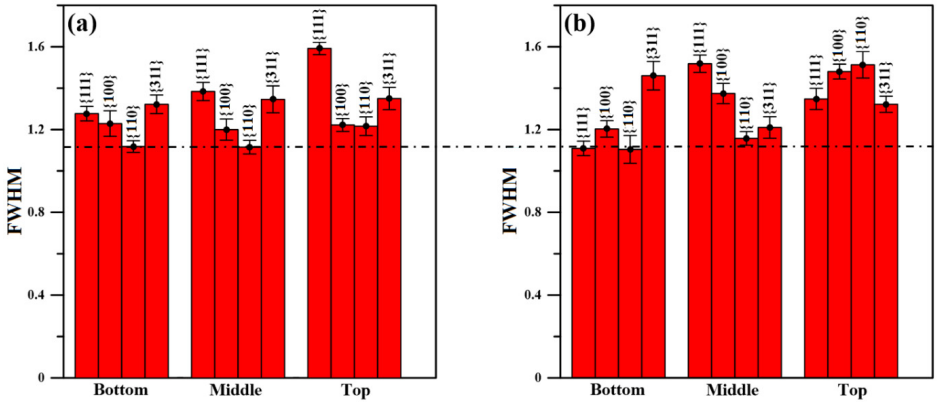

Figure 6. FWHM of the Al phase of the (**a**) L200 and (**b**) L400 specimens.

The obtained values were compared to the standardized ones given in the ICDD database for polycrystalline aluminum and silicon samples. The lattice constant of the Si phase remains about the same in the range of 5.430–5.435 Å throughout all experiments regardless of the position of the specimen the sample was taken from, as well as the dimension of the manufactured detail, which corresponds almost ideally to the standard value of 5.430 Å presented in the database. This means that during the experiments, the silicon phase did not undergo any change due to the high thermal input of the welding heat source. In contrast, the aluminum phase did exhibit a slight increase in the lattice constant in both cases from the standard value of 4.049 Å. The calculated values are summarized in Figure 7. Although an increase in the lattice constant of both specimens is observed, slightly higher values are observed for the larger L400 specimen. This corresponds to a slightly higher thermal input compared to the smaller specimen, which can be explained by a higher deposition time. The theoretical calculations presented in this work were confirmed experimentally by Nakashima [30] who noticed an increase in the lattice constant due to the increase in the temperature of heating of aluminum samples. Despite the slight increase in the lattice constant of both specimens, no significant change compared to the standard value was observed indicating that both specimens have similar crystal properties.

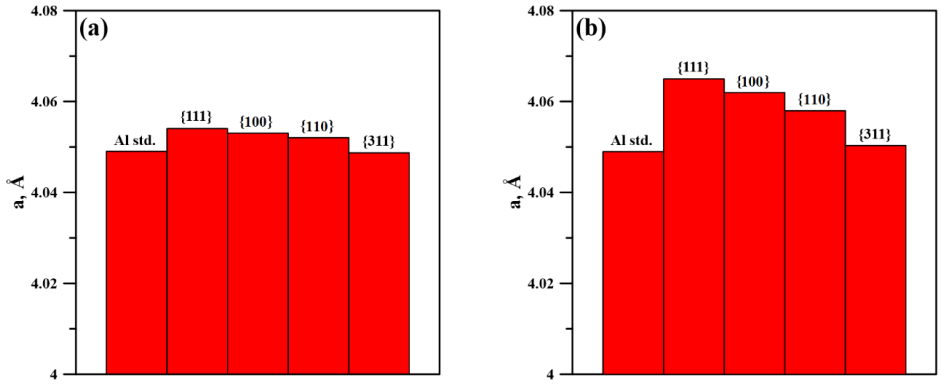

Figure 7. Lattice constant a (Å) of the Al phase of the (**a**) L200 and (**b**) L400 specimens.

Since the specimens were built using similar technological conditions, there is no visible difference in their shape; however, a slight difference in their thickness can be noticed. This is confirmed by the optical microscopic images of the cross-sections of the L200 (Figure 8a) and the L400 (Figure 9a) specimens. The cross-section of the L400 specimen is 1 mm thicker than the cross-section of the L200 specimen. Furthermore, the thicknesses of the larger and the smaller specimens at the beginning of the manufacturing process were 9 mm and 8 mm, respectively, which then increased to 10 mm and 9 mm. This is attributed to the accumulation of heat in the specimens, which leads to an increase in the

layer deposition temperature. These results are in complete agreement with the results obtained by the authors of [31] who also observed the same tendency.

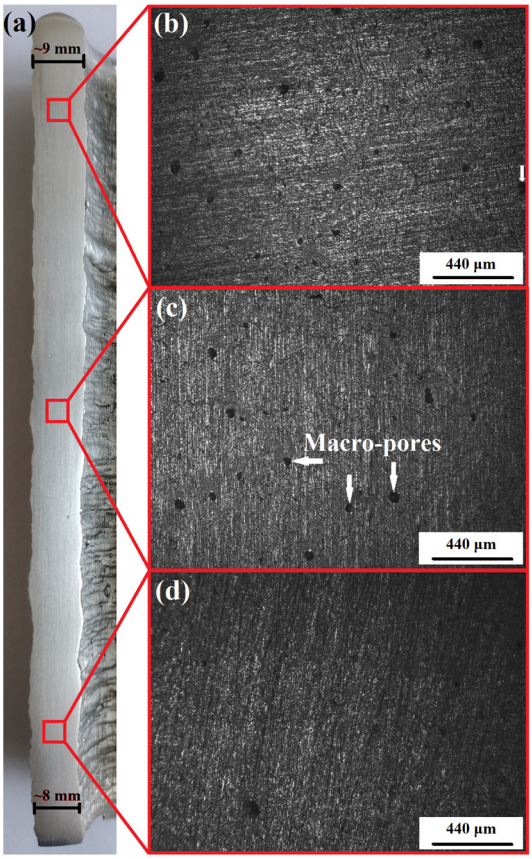

Figure 8. Macroscopic image of the cross-section of the L200 specimen (**a**) and optical images of the top (**b**), middle (**c**), and bottom sections (**d**) of the same specimen.

Figure 8b–d depict optical images taken from the top, middle, and bottom sections of the L200 specimen. An increasing number of macro-pores is observed with the increase in the height of the specimen. The pores in the images are indicated using white markers (arrows). Figure 8b–d show optical images of the top, middle, and bottom sections of the cross-sectional area of the L400 sample. The images indicate that in this case, no change in the concentration of macro-pores was observed at the different stages of specimen build-up. In addition, the concentration of pores in this specimen is considerably lower than that of the L200 specimen. At the initial stages of build-up, the smaller specimen has a concentration of macro-pores closely similar to that of the L400 specimen. However, this changes with an increase in height. As Anyalebechi et al. [32] have noticed, the solubility of gases into aluminum increases with an increase in temperature. During the process of WAAM, an increase in the layer deposition temperature is also noticed. This means that with the increase in the height of the specimens, the likelihood of gas incorporation in their structure increases. The adsorption of gases in the molten zone during gas metal arc welding is a function of the solidification speed. The lower the solidification speed, the higher the diffusion of gases is, which helps to release as much entrapped gases within the structure as possible. Evidently, in the case of the smaller specimen, the solidification speed is too fast, which leads to the formation of a higher concentration of macro-pores. In the initial stages of build-up, the amount of pores observed in the structure is similar to the amount of pores observed within the structure of the larger specimen, which is attributed to the lower temperature of the specimen at that stage, and thus the reduced solubility of gases in the aluminum component.

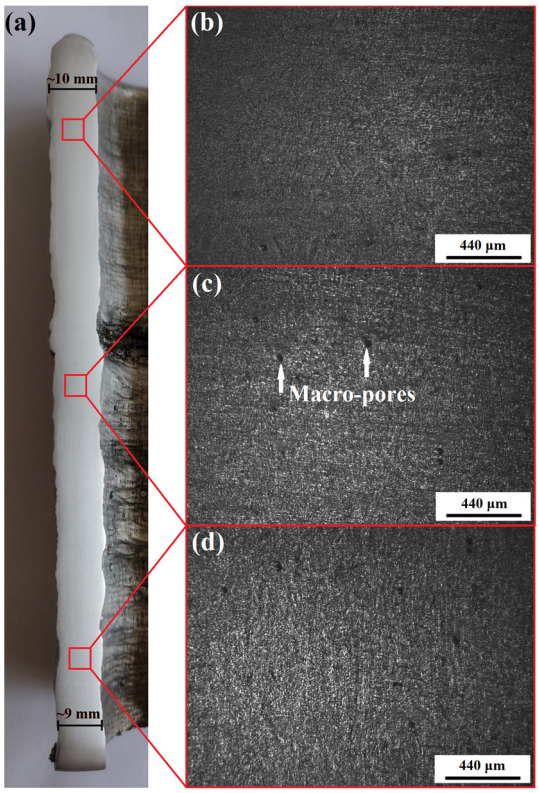

Figure 9. Macroscopic image of the cross-section of the L400 specimen (**a**) and optical images of the top (**b**), middle (**c**), and bottom sections (**d**) of the same specimen.

Figure 10 shows optical images taken from the side wall of the L200 specimen at the different stages of build-up. The bottom section of the specimen is depicted in Figure 10c, and a zoomed area of the same sample is shown is Figure 10f. The same approach was used for the middle (Figure 10b,e) and top (Figure 10a,d) sections. Clearly visible eutectic formations consisting of αAl + Si were observed oriented towards the build-up direction of the specimen. A decrease in the concentration of those formations at the top of the specimen and an increase in the size of the aluminum grains were also noticed. The average area of each individual αAl grain at the bottom of the specimen is about 121 μm^2, at the middle the values reach 305 μm^2, and at the top they are 550 μm^2.

Figure 11 depicts optical images from the side wall of the L400 specimen taken from the top (Figure 11a), middle (Figure 11b), and bottom (Figure 11c) sections of the specimen along with zoomed images corresponding to the same areas (Figure 11d–f). Similar to the L200 specimen, eutectic formations within which the secondary Si phase resides in the form of an αAl + Si solution were observed, which are also oriented towards the direction of build-up of the specimen. However, unlike the L200 specimen in this case, no noticeable change in the concentration of the eutectic formations was observed and thus no change in the size of the aluminum grains. The grains in the bottom, middle, and top sections of this specimen have average areas of 171 μm^2, 185 μm^2, and 233 μm^2, correspondingly.

Figure 12 depicts optical images taken from the cross-section of the L200 specimen corresponding to the bottom (a), middle (b), and top (c) sections. These images confirm the decrease in the concentration of the eutectic formations and the increase in the size of the aluminum grains.

Figure 13 shows optical images taken from the cross-section of the L400 specimen corresponding to the bottom (a), middle (b), and top (c) sections. These images confirm that regarding the L400 specimen, no obvious change in the size of the aluminum grains is observed, and thus no substantial difference in the size and concentration of the eutectic structures.

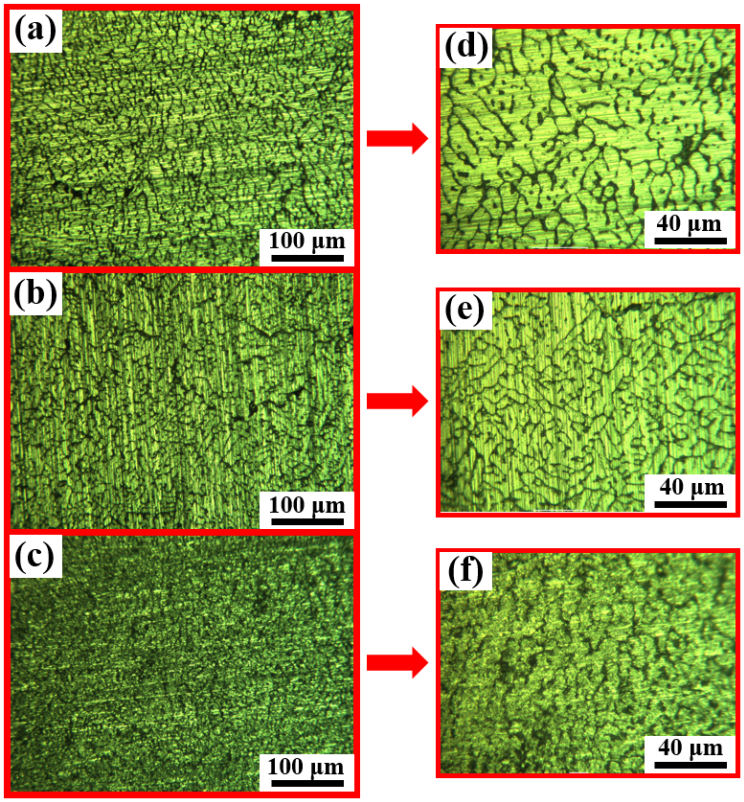

Figure 10. Optical images of the side wall of the L200 specimen taken from the top, middle, and bottom (**a**–**c**) correspondingly with zoomed areas of the same locations shown in (**d**–**f**).

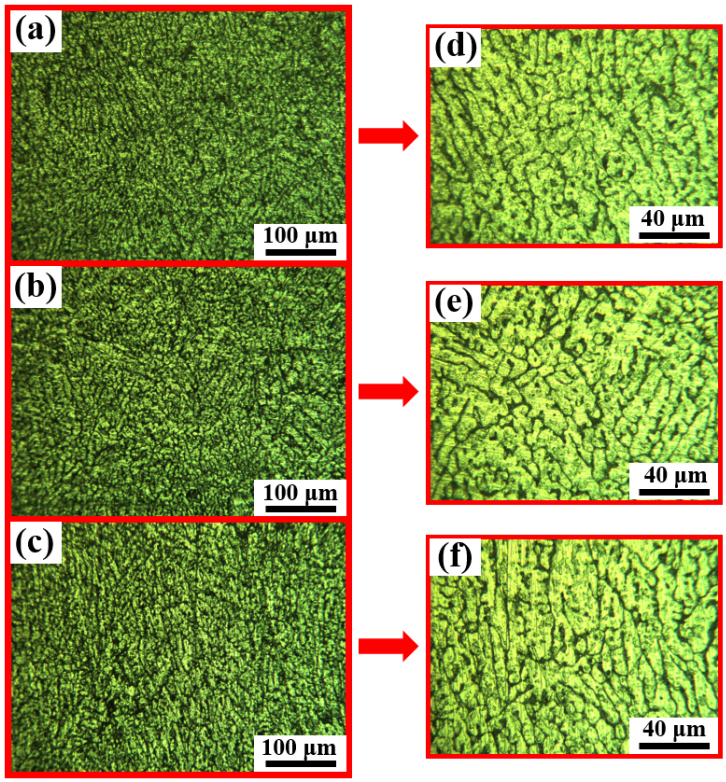

Figure 11. Optical images of the side wall of the L400 specimen taken from the top, middle, and bottom (**a**–**c**) correspondingly with zoomed areas of the same locations shown in (**d**–**f**).

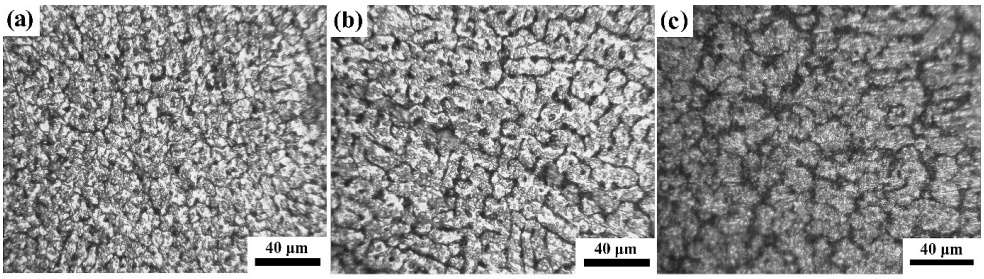

Figure 12. Optical images of the cross-section of the L200 specimen parallel to the trajectory of the weld torch corresponding to the bottom (**a**), middle (**b**), and top (**c**) sections of the same specimen.

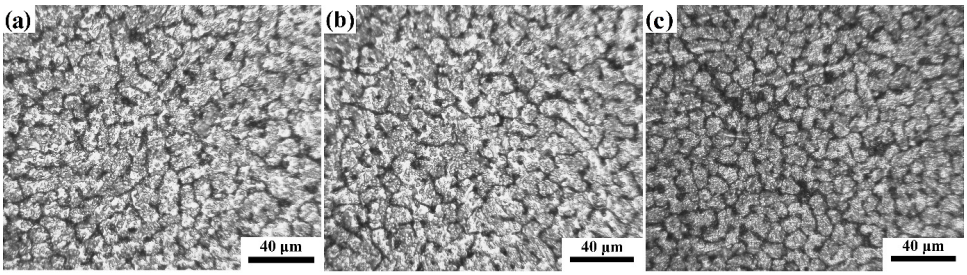

Figure 13. Optical images of the cross-section of the L400 specimen parallel to the trajectory of the weld torch corresponding to the bottom (**a**), middle (**b**), and top (**c**) sections of the same specimen.

The microstructure of all samples was closely studied using scanning electron microscopy. The results of the experiments are shown in Figures 14–19. The bottom section of the L200 specimen was studied and the obtained images are presented in Figure 14. Figure 14a presents a macro image of the studied area, where a large macro-pore is observed. A small quantity of smaller irregularly shaped pores along with some contaminants on the surface are also both observed in Figure 14a,b. A closer inspection of the surface of the sample (Figure 14b,c), a double-phase structure comprised of pure aluminum and αAl + Si eutectic structures, was observed. These structures consist of a mixture of fibrous and irregularly shaped eutectic formations.

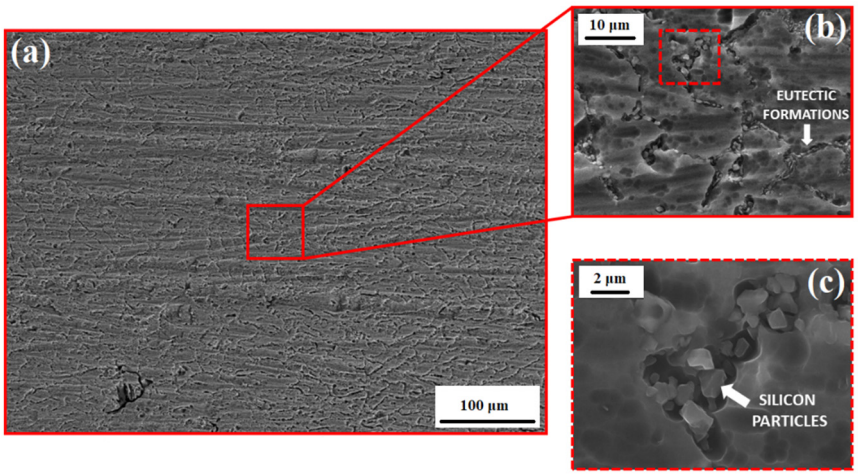

Figure 14. SEM images of the bottom sample of the L200 specimen: (**a**) BSE mode image at 500x zoom; (**b**) SE mode image of the same sample at 5000x; and (**c**) SE mode image at 20,000x.

Figure 15a presents a macro image of the studied sample taken from the middle of the L200 specimen. Once again, a macro-pore is observed along with a small quantity of smaller pores. In regard to the microstructure (Figure 15b,c), a double-phase structure of Al and Si is observed. In Figure 15b, a small undissolved Fe particle is observed located amidst the secondary phase.

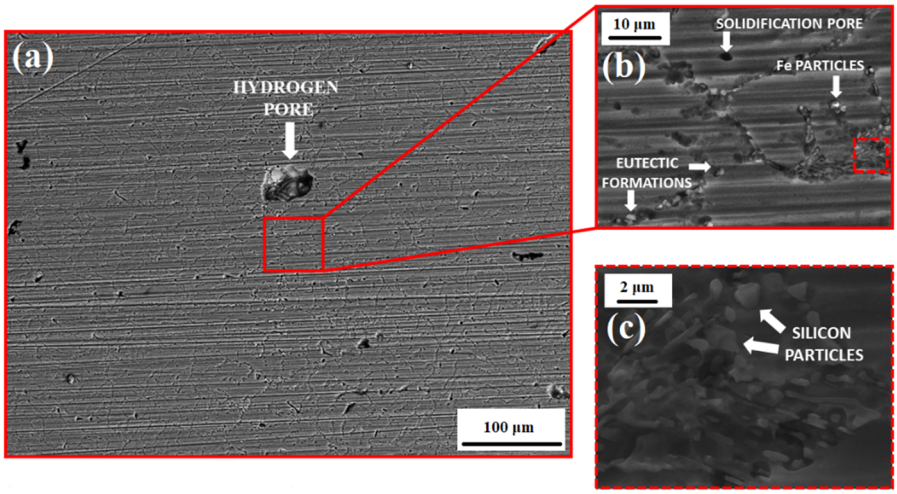

Figure 15. SEM images of the middle sample of the L200 specimen: (**a**) BSE mode image at 500x zoom; (**b**) SE mode image of the same sample at 5000x; and (**c**) SE mode image at 20,000x.

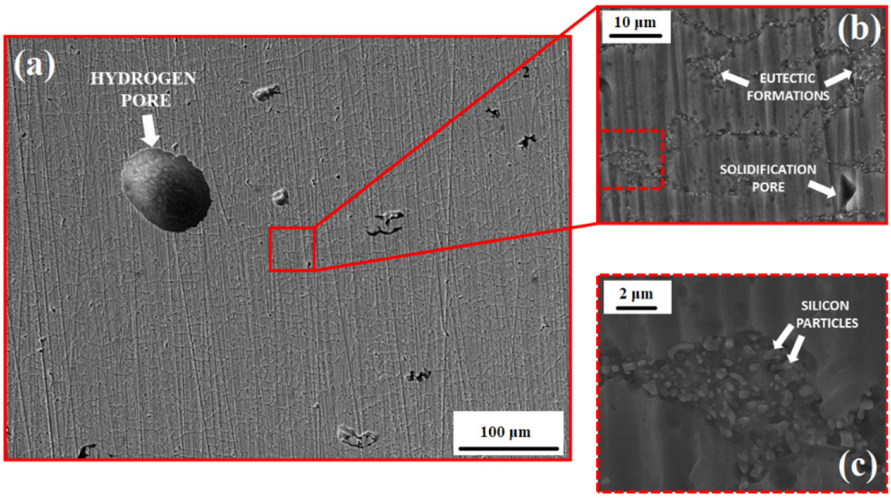

Figure 16. SEM images of the top sample of the L200 specimen: (**a**) BSE mode image at 500x zoom; (**b**) SE mode image of the same sample at 5000x; and (**c**) SE mode image at 20,000x.

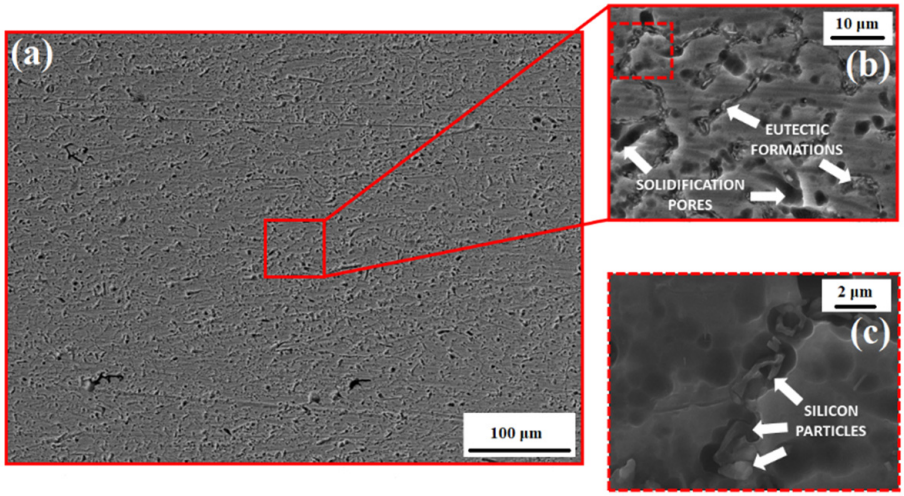

Figure 17. SEM images of the bottom sample of the L400 specimen: (**a**) BSE mode image at 500x zoom; (**b**) SE mode image of the same sample at 5000x; and (**c**) SE mode image at 20,000x.

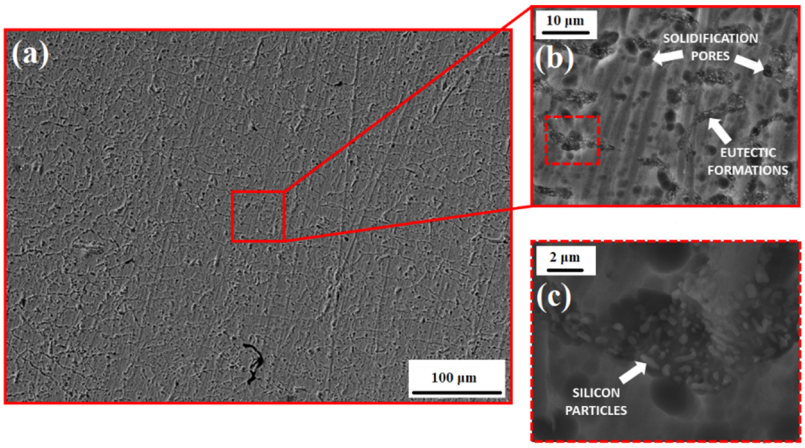

Figure 18. SEM images of the middle sample of the L400 specimen: (**a**) BSE mode image at 500x zoom; (**b**) SE mode image of the same sample at 5000x; and (**c**) SE mode image at 20,000x.

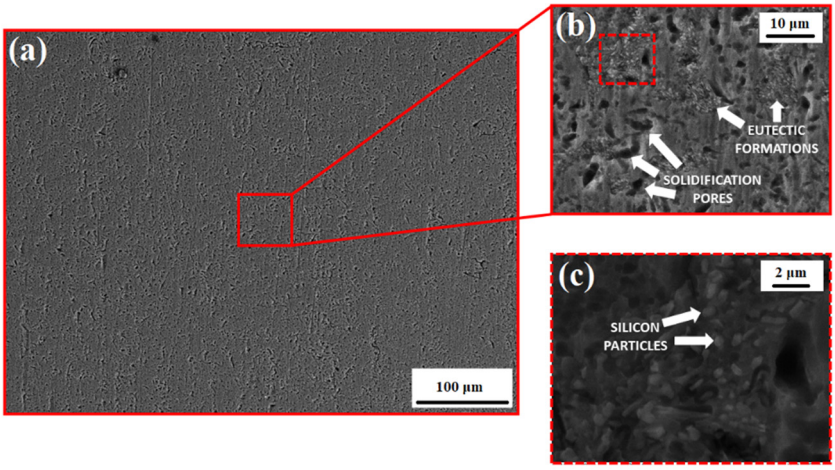

Figure 19. SEM images of the top sample of the L400 specimen: (**a**) BSE mode image at 500x zoom; (**b**) SE mode image of the same sample at 5000x; and (**c**) SE mode image at 20,000x.

As with the previous images, Figure 16a shows a macro image of the studied area of the sample taken from the bottom of the L200 specimen, and Figure 16b,c show higher magnification images of the structure of the sample. In this case, no macro-pores are visible and the eutectic formations visible in Figure 16b,c still possess a combination of fibrous and irregular eutectic structures.

Figures 17a, 18a and 19a present SEM images corresponding to the bottom, middle, and top sections of the L400 specimen. A higher concentration of defects is observed in all cases compared to the L200 specimen. Figures 17b, 18b and 19b present magnified images of the studied zones. They confirm the presence of a much higher concentration of defects in the structure of this specimen compared to the shorter one. These defects are in the form of small micro-pores, which occur during the process of welding due to the "shrinkage" of the material during the solidification stage. The slower solidification speed of the larger specimen is another cause of formation of solidification pores. Furthermore, it is possible for gas molecules to be still entrapped in the structure of the specimen regardless of its higher efficiency in the diffusion of gases compared to the L200 one. The presence of such molecules worsens the formation of bonds between separate aluminum particles. In the case of the larger L400 specimen, a slight increase in the concentration of defects was observed at the different stages of build-up.

Figure 20 depicts the results of the EDX mapping analysis performed at the bottom (a), middle (b), and top (c) sections of the L200 specimen. All images confirm that the observed structures with the optical and SEM analyses are indeed a combination of an αAl phase

and a secondary eutectic structure consisting of αAl + Si. A zoomed image of the middle section (Figure 20d) was taken due to the presence of an irregular particle in the structure of the secondary phase. The performed EDX in the area of that particle (Figure 20e) indicates that this particle is made out of iron. The welding wire manufacturer indicates that the welding wire consists of a 0.49 wt% of Fe. The presence of Fe in the structure of aluminum alloys is quite contradictory. Typically, iron is considered as an impurity that plagues aluminum alloys and leads to a worsening of the mechanical properties of the alloys due to the formation of the brittle β-Al_5FeSi phase that reduces their ductility [33]. In addition, due to the much higher melting temperature of Fe compared to aluminum and due to the much lower fusion energy of that material, the process of formation of the β-Al_5FeSi phase is characterized by a slow solidification speed, such as the one achieved during casting processes [33]. However, despite the arc welding process not having speeds of solidification of the molten pool as high as welding methods that employ high energy fluxes, such as laser beam welding (LBW) [34] or electron beam welding (EBW) [35], the process is still characterized by significantly higher solidification speeds compared to standard processes of specimen formation such as casting [33,36]. This is the reason why the Fe particles observed in the structure of the alloy are in the form of undissolved particles and not in the form of the β-Al_5FeSi phase. The iron in the wire uses a secondary phase moderator, which improves the stability of formation of the secondary silicon phase.

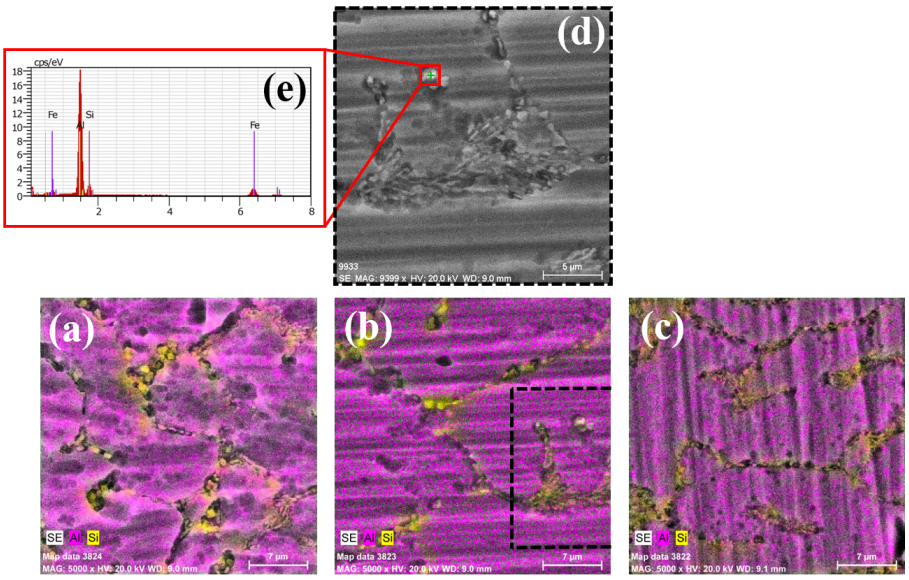

Figure 20. EDX results for the (**a**) bottom, (**b**) middle, and (**c**) top sections of the L200 specimen with a zoomed image of a highly silicon concentrated area (**d**) and an EDX spectrograph (**e**) taken in a point.

Figure 21 shows the results of the EDX mapping analysis performed for the bottom (a), middle (b), and top (c) sections of the L400 specimen. Once again, a double-phase mixture consisting of a pure aluminum phase and a eutectic αAl + Si structure is observed. The secondary eutectic structure has no detected irregularities in its composition. A high quantity of small pores was observed in this case, confirming the observed tendency in the SEM images of the L400 specimen to have a higher concentration of defects compared to the L200 one.

In the case of the L200 specimen, the concentration of silicon at its bottom is 6.69 wt%. The concentration of silicon decreases linearly, with the increase in the height of the specimen being 5.42 wt% in the middle section and 5.04 wt% in the top one. The results confirm those obtained while analyzing the optical micrographs. In comparison, there is no significant change in the concentration of silicon in the structure of the L400 specimen varying between 4.97 and 5.35 wt%.

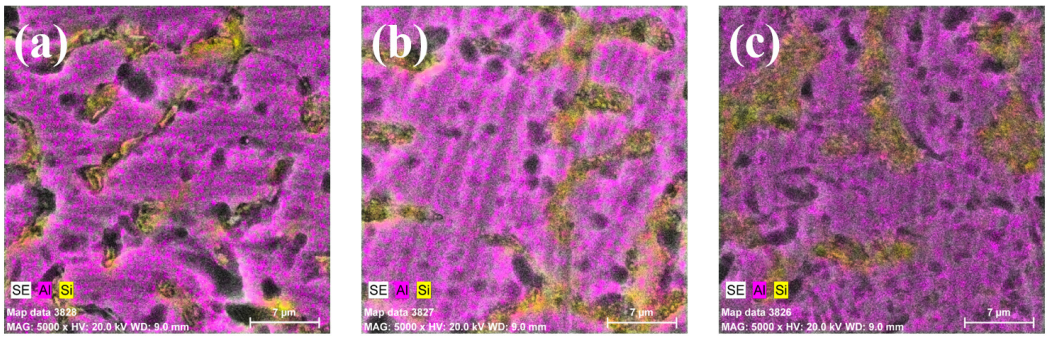

Figure 21. EDX results for the (**a**) bottom, (**b**) middle, and (**c**) top sections of the L400 specimen.

The microhardness according to the Vickers scale is shown in Figure 22. The results presented in it are obtained for specimens of both lengths at different stages of specimen build-up. The lowest obtained value was 46.9 ± 1.1 HV0.1, corresponding to the top section of the L200 specimen. The highest average microhardness value was 55.8 ± 2.5 HV0.1 and it was observed at the bottom of the L200 specimen. Considering the smaller specimen, an obvious decrease in the microhardness was observed following the direction of build-up. Comparably, a decrease in the Vickers hardness of the L400 specimen following the same measuring strategy was observed; however, the observed decrease curve is much flatter compared to that of the smaller specimen. The decreasing character of the microhardness is primarily attributed to the increase in the size of the aluminum grains with the increase in the specimens' heights. As discussed above, the increase in the size of the grains is much more pronounced in the case of the smaller specimen. Pramod et al. [22] also reported a decrease in the microhardness of an Al4043 CMT+P manufactured circular-shaped specimen. This is in agreement with the current results. In previous studies, the possibility of increasing the microhardness of wall-shaped specimens, manufactured in the cold arc pulse mode with an Al4043 welding wire, with an increase in their height was studied [24]. The results also suggested that the variation in the type of silicon eutectic structures and their concentration in the primary αAl solid solution were highly responsible for the variation in the microhardness.

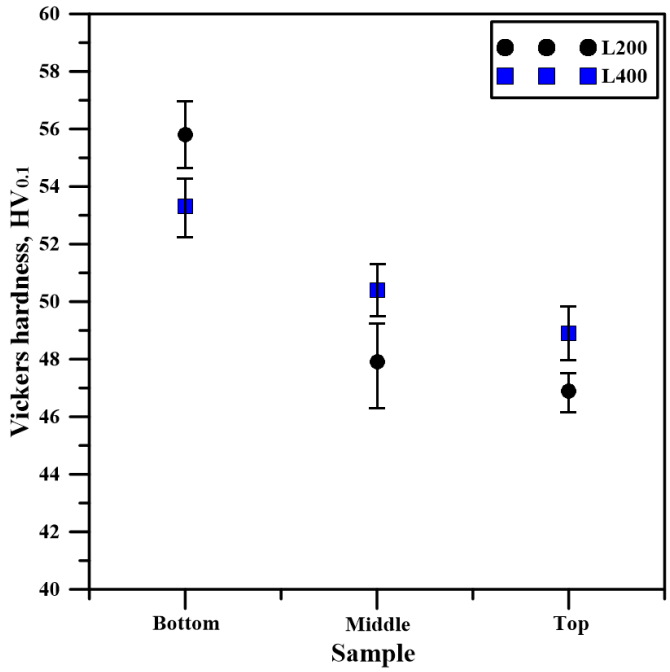

Figure 22. Microhardness results for the samples taken from the top, middle, and bottom sections of the specimens.

Along with the microhardness experiments, tensile strength tests were performed for both specimens in the vertical and horizontal orientations. The samples are shown in Figures 23 and 24, and the results are presented in Table 4. An average ultimate tensile strength (σUTS) of 155 MPa was observed while studying the vertical samples of the L400 specimen, and a σUTS of 161 MPa was observed while studying the horizontal samples of the same specimen. In regard to the L200 specimen, an average ultimate tensile strength of 158 MPa was achieved in the vertical direction and 163 MPa in the horizontal one. As far as the yield strength (σYS) is concerned, average σYS values of 61 MPa and 60 MPa were achieved for the L400 sample in the vertical and horizontal directions, respectively. The L200 specimen had an average yield strength in the vertical direction of 57 MPa and 64 MPa in the horizontal one. The average elongation (ε) values in the vertical direction of the L400 and L200 specimens were 14.19% and 12.31%, accordingly. And, in the horizontal directions of both specimens, average values of 17.8% and 17.3% were detected, corresponding to the L400 and L200 specimens. In all cases, the samples broke after applying an average force of 13 kN.

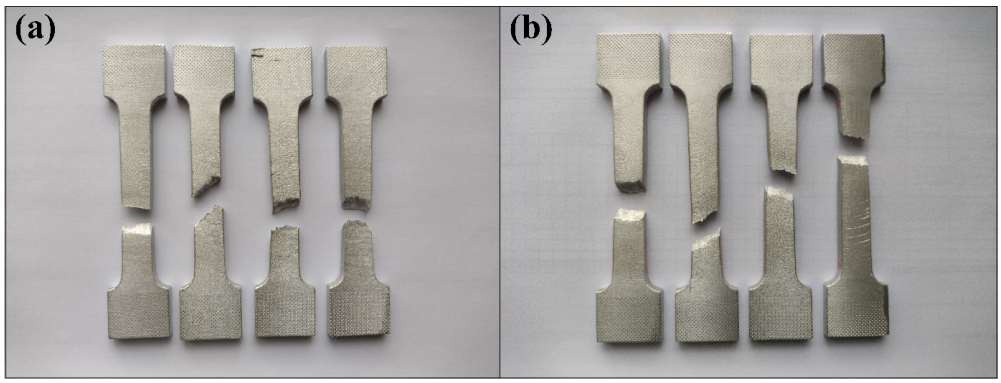

Figure 23. Tensile test samples of the L200 specimen of the (**a**) vertical and (**b**) horizontal directions of specimen build-up.

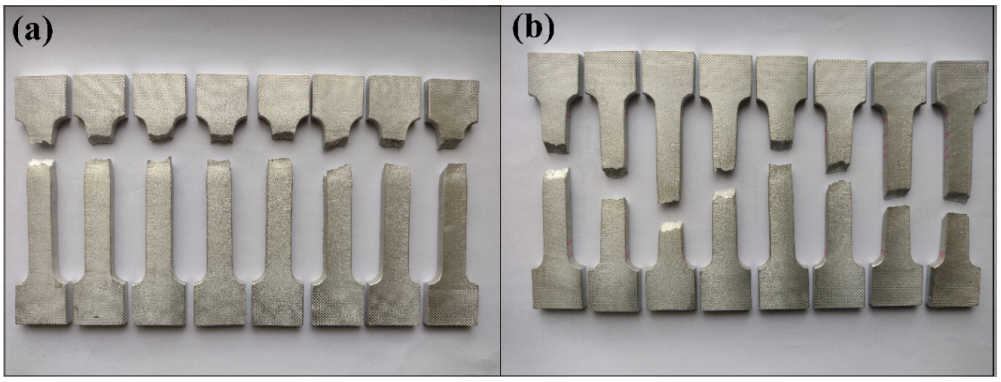

Figure 24. Tensile test samples of the L400 specimen of the (**a**) vertical and (**b**) horizontal directions of specimen build-up.

Table 4. Tensile test results for both specimens.

Specimens	Direction of Build-Up	σ_{YS}, MPa	σ_{UTS}, MPa	ε, %
L200	vertical	57	158	12.3
L400		61	155	14.2
L200	horizontal	64	163	17.3
L400		60	161	17.8

Interestingly, a tensile test breaking pattern can be observed where the L400 vertical samples (Figure 24a) break at the exact same area of the samples, namely closer towards the top of the specimen. This can be explained by the increase in the concentration of internal macro-defects with the increase in the height of this specimen, which can be confirmed by optical and SEM observations. These types of defects are known to be the primary cause of reduction in the mechanical properties of WAAM specimens [37]. When the L200 specimen was concerned, the breaking pattern of the vertical samples (Figure 23a) was seemingly random. The L400 samples tested in the horizontal direction (Figure 24b) of specimen build-up show a similar tendency to the horizontal ones (Figure 23b) of the L200 specimen.

4. Discussion

As it is known, the thermal conductivity of metals decreases with the increase in the temperature. Due to the increase in the interpass temperature, the thermal conductivity of the material decreases leading to the stabilization of the process of heating up and cooling (stabilization of the thermal gradients).

When comparing the two specimens, the L200 one has a significantly lower amount of micro-pores within its entire volume, while the L400 specimen has a significantly larger quantity of this kind of defect. The images also include the formed secondary αAl+Si structure in the form of eutectic formations. In all cases, the eutectic formations are of the anomalous kind combining both irregularly shaped and fibrous shaped structures. As determined by previous researchers [38], the type and concentration of eutectic structures were correlated directly to the resultant mechanical characteristics of the built components. As observed in previous research [24], the formation of fibrous eutectic structures within the volume of the specimens led to an increase in their hardness. This improvement in the microhardness is attributed to the orderly nature of the eutectic structure which acts as a reinforcement for the aluminum matrix. In the present work, a more scattered formation of eutectic structures was observed at the bottom of the specimens due to the faster speed of cooling at the initial stages of build-up. This is caused by the lower interpass temperature. The increase in the same leads to an increased life of the melt pool, which improves the formation of eutectic clusters in the structure of both specimens. Despite this trend, no major change in the type of the eutectic structures was observed, and thus no direct influence of the type of eutectics on the resultant mechanical properties was observed either.

In regard to the microhardness of the specimens, as discussed above, this shows a decreasing trend in the case of both the L200 and the L400 specimens. No variance in the microhardness was observed while studying different sections of the specimens (faceplate or cross-section) at the same stages of build-up. The presented results indicate that a higher accumulation of heat was observed in the case of the smaller L200 specimen compared to the large one. This is most probably attributed to the much smaller thermal efficiency of that specimen, which is a function of its volume. This leads to an increase in the interpass temperature and thus to accelerated micro-volume changes. This leads to an increase in the micro-volumes from 121 μm^2 to 550 μm^2, which is a 4.5x increase compared to the micro-volume changes that occur in the L400 specimen when their size increases from 171 μm^2 to 233 μm^2, which is only a 1.4x increase. As a result, the microhardness of the L200 specimen decreases more rapidly compared to the L400 specimen. Regardless of all this, all obtained values are highly similar, almost within the margin of error of the measuring method. Of course, this is attributed to the same observed trend in the change in the microvolumes. In addition, a higher concentration of micro-pores is observed in the structure of the L400 specimen, which results in a decrease in the microhardness values closer to those of the L200 one. The Vickers hardness of the specimens varies between about 40 and 60 HV in all cases, which is in agreement with data previously obtained by the authors of [20].

Due to the different thermophysical properties of the specimens, such as the different thermal efficiency, the resultant microstructure and structural defects were different. Fur-

thermore, due to the larger physical size of the L400 specimen, a much longer deposition process was observed. The increased time of applying heat to that specimen led to an increase in the lifetime of the melt pool, which resulted in the increased formation of micro-pores within the structure of the specimen but improved the natural processes of gas diffusion, resulting in the reduced formation of macro-pores. In comparison, a very tiny amount of micro-pores was observed in the structure of the L200 specimen due to the higher solidification speed; however, the process of the diffusion of gases was hindered by the rapid solidification rate. The adsorption of gases is related both to the surrounding environment and the affinity of the material to adsorb specific types of gases. For example, aluminum shows a low affinity towards the adsorption of gases such as oxygen or nitrogen. However, it exhibits a large affinity towards the adsorption of hydrogen in its structure. Due to this, it is a common theory that the macro-pores also observed in this work are caused by the adsorption of hydrogen in the structure of the specimens. During the welding process, hydrogen can be found in the surrounding air, in the form of condensed moisture atop the welding wire, or within the structure of the welding wire itself in small quantities [39]. Most commonly during MIG/MAG welding, hydrogen is introduced in the volume of the weld through its adsorption from the surrounding air. Despite the use of protective gas while welding, depending on the lifetime of the weld pool, the same can still be in a semi-liquidus state after the torch, with the protective gas flow passed over its perimeter. In this state, the weld pool is still capable of adsorbing gases. This means that the adsorption of gases is a function of the solidification speed. During the current experiments, hydrogen-related pores were potentially noticed in the cross-section of the L200 and the L400 specimens, using both optical microscopy and scanning electron microscopy (SEM). Furthermore, there is a potential possibility that some of the formed micro-pores within the structure of the specimens are caused by the entrapment of separate molecules of gases (most probably hydrogen); however, the present work is insufficient to prove that. The lower solidification speed of the L400 specimen led to the formation of a structure with a reduced amount of macro-defects due to the improved diffusion of gases; however, if some residual molecules of hydrogen remained in the weld pool, they caused a poor recombination of the aluminum grains and thus the formation of micro-defects. Other possible reasons for the high concentration of micro-defects in the volume of the L400 specimen are the low solidification speed and the high accumulation of heat in that specimen. The current observations are in agreement with the ones made by Derekar et al. [39] who confirm that the increase in the interlayer temperature with the increase in the height of the specimen results in an increase in the concentration of macro-pores. Wang et al. [40] reported that an increased formation of defects can occur in the zone between each separate layer. Such a trend, however, was not observed during the present research. The concentration of pores remains the same at each stage of manufacturing of the oval-shaped specimens. Additionally, the presence of macro- and micro-defects in the structure of both specimens, regardless of concentration, suggests that in both cases the solidification speed is too low.

The tensile strength of the produced specimens is of extremely high importance to their application in the industry. As previously discussed, the obtained results indicate that there is no significant difference between the tensile properties of both the L200 and the L400 specimens, despite the different types of defects observed in their structures and the difference between the structures themselves. Only a very slight improvement in the tensile properties in the vertical direction of build-up of the specimen was observed in the case of the larger L400 specimen due to the lower gradient of the increase in the grain size. Different values of elongation were detected for both specimens while performing the experiments that depended on the orientation of the build-up. The samples taken from the horizontal direction of build-up exhibit slightly higher elongation values compared to the ones studied in the vertical orientation of component manufacturing. This signifies that a much better thermal balance is achieved during the formation of a single layer, as compared to the layer-by-layer deposition of the subsequent layers. Higher uniformity of

the built specimens is observed in the horizontal direction of build-up, which correlates to the direction of welding, as compared to the vertical direction of build-up. Due to this, the ductility of the specimens in the horizontal direction is slightly higher compared to the ductility in the vertical direction. In either case, a study examining the correlation between the tensile properties and the microhardness of aluminum specimens was proposed [41], and it indicated that the relation between the UTS and the microhardness is linear. With the increase in microhardness, the UTS increases as well. The data obtained by Salazar-Guapuriche [41] are in agreement with the data obtained in the present work regarding the UTS/HV ratio. Wieczorowski et al. [42] have studied the influence of the different time before each subsequent layer's deposition on the mechanical properties of the specimens. They have found that an increase in the wait time results in a decrease in the interpass temperature and the tensile samples' elongation. However, the specimens studied in [41] were all built to the same size. This indicates that the decrease in the elongation of the L200 specimen compared to the L400 one was most probably caused by the increase in the grain size of that specimen with the increase its height. This steady increase in the grain size leads to the formation of a structure with uneven elastic and plastic properties. The increase in the size of the Al grains of the αAl solid solution improved the plastic properties of the specimen but decreased its elastic ones. This is the most probably the cause of the decrease in the elongation of the vertical samples of the L200 specimen compared to the L400 one. In any case, the tensile properties and the microhardness of both specimens are lower than expected for specimens manufactured using the Al4043 alloy. This is caused by the increased formation of macro- and micro-defects within their structure and also by the unstable structure of the smaller specimen. Further optimization of the process has to be performed in order to improve the mechanical characteristics and the microstructure of the obtained components.

The physical dimensions and geometry of the built component have a direct effect on the amount of post-processing required for finalizing the manufacturing process and coming up with the output product. This also has an effect on the manufacturing costs and the cost of the final product. An ongoing issue with the GMAW technique is the different temperature levels of the specimen during its manufacturing. Initially, the interpass temperature is about 30–35 °C, which increases to up to 60–70 °C. This increases the deposition temperature. The higher deposition temperature leads to the formation of a wider melt pool, and thus to an increase in the thickness of the specimens. This difference between the thickness of the specimens' cross-section increases the cost of machining and increases the waste of material during post-production. A similar difference in the thickness of WAAM built components was also observed by the authors of [21].

5. Conclusions

The results of the current work led to the formation of the following conclusive statements:

(1) During the WAAM of Al4043 components, a number of processes occur as follows: heat transfer during heating–cooling cycles realized by thermal conductivity and convection; volume changes; partial remelting of the underlying layer and recovery of lattice imperfections; separation of Si precipitates from the oversaturated αAl solid solution, etc.;
(2) The structure of the specimens consists of primary αAl grains and a eutectic mixture of αAl + Si;
(3) The occurring crystallization and recovery processes are accompanied by a formation of nano-sized crystal defects. In the present work, no significant differences between these defects were observed as a function of the physical size of the manufactured specimens;
(4) Due to the higher solidification speed of the L200 specimen, an increased concentration of spherical-shaped macro-pores was observed, which are presumed to be related to hydrogen absorption;

(5) Due to volume changes during the heating–cooling cycles, a number of irregularly shaped microscopic sized pores have been formed in the structure of both specimens. Due to the lower rate of volume changes in the L400 specimen, a higher concentration of micro-pores was obtained;
(6) The smaller specimen showed a tendency of higher thermal accumulation during the manufacturing process, resulting in an increase in the size of the aluminum grains. The larger L400 specimen had an improved thermal efficiency leading to a more uniform process and a less pronounced change in the size of the aluminum grains;
(7) The increase in the size of the primary αAl grains led to the formation of a decreasing trend for the microhardness values of both specimens with an increase in their height;
(8) Despite the different microstructures and defect formation, the specimens exhibited similar mechanical properties with the smaller one having only slightly worse ones compared to the larger one;
(9) The components investigated in this work satisfy the requirements for good adhesion and the absence of cracks. More can be desired for the structure and mechanical properties, which are predominantly hindered by the formation of microscopic pores within the structure of the specimens. Measures need to be taken for a reduction in the formation and concentration of such structural defects. The optimization of the technological conditions and production of components with improved mechanical properties will be a purpose of future investigations.

Summarizing the results of the current work, it can also be concluded that when AlSi hypoeutectic alloys are concerned, in particular Al4043 (AlSi5), there is a substantial difference in the degree of volume changes depending on the volume of the specimen. However, there is no significant evidence that increasing the size of the specimens should lead to a major change in the mechanical properties of the manufactured components. Furthermore, it turns out that it is actually more beneficial to produce larger components using the GMAW technique for WAAM in the cold arc pulse mode, as supposed to smaller components that are not as thermally efficient.

Author Contributions: Conceptualization, G.K., S.V., R.O. and N.D.; methodology, S.V., G.K., M.O., R.O., I.M., N.D. and V.M.; validation, G.K., S.V., M.O., N.D. and I.M.; formal analysis, G.K., M.O., I.M. and A.N.; investigation, G.K., M.O., N.D., I.M. and A.N.; data curation, G.K., M.O., I.M. and A.N.; writing—original draft preparation, G.K.; writing—review and editing, S.V., G.K., N.D., I.M. and V.M.; funding acquisition, S.V., R.O. and V.M. All authors have read and agreed to the published version of the manuscript.

Funding: This research was funded by the Bulgarian National Science Fund, grant number KP 06-DO 02/1 (2019).

Data Availability Statement: The data presented in this study are available on request from the corresponding author, due to legal and ethical reasons.

Acknowledgments: The authors would like to express their deepest gratitude to Ivanka Iordanova for invaluable guidance and motivation for scientific growth.

Conflicts of Interest: The authors declare no conflicts of interest.

References

1. Gibson, I.; Rosen, D.; Stucker, B.; Khorasani, M. *Additive Manufacturing Technologies*; Springer International Publishing: Cham, Switzerland, 2021.
2. Rodrigues, T.; Duerte, V.; Miranda, R.; Sanos, T.; Oliveira, J. Current Status and Perspectives on Wire and Arc Additive Manufacturing (WAAM). *Metals* **2019**, *12*, 1121. [CrossRef]
3. Singh, S.; Khanna, P. Wire arc additive manufacturing (WAAM): A new process to shape engineering materials. *Mater. Today Proc.* **2021**, *44*, 118–128. [CrossRef]
4. Treutler, K.; Wesling, V. The Current State of Research of Wire Arc Additive Manufacturing (WAAM): A Review. *Appl. Sci.* **2021**, *11*, 8619. [CrossRef]
5. Jia, Q.; Gu, D. Selective laser melting additive manufacturing of Inconel 718 superalloy parts: Densification, microstructure and properties. *J. Alloys Compd.* **2014**, *585*, 713–721. [CrossRef]

6. Spears, T.; Gold, S. In-process sensing in selective laser melting (SLM) additive manufacturing. *Integr. Mater. Manuf. Innov.* **2016**, *5*, 16–40. [CrossRef]
7. Gasser, A.; Backes, G.; Kelbassa, I.; Weisheit, A.; Wissenbach, K. Laser Metal Deposition (LMD) and Selective Laser Melting (SLM) in Turbo-Engine Applications. *Laser Tech. J.* **2010**, *7*, 58–63. [CrossRef]
8. Katayama, S. *Handbook of Laser Welding Technologies*; Woodhead Publishing Limited: Cambridge, UK, 2013.
9. Liu, R.; Wang, Z.; Sparks, T.; Liou, F.; Newkirk, J. Aerospace applications of laser additive manufacturing. In *Laser Additive Manufacturing*; Woodhead Publishing Series in Electronic and Optical Materials; 2017; pp. 351–371.
10. Sudnik, V. *Arc Welding*; InTech: Riijeka, Croatia, 2011.
11. Weman, K.; Linen, G. *MIG Welding Guide*; Woodhead Publishing Limited: Cambridge, UK, 2006.
12. Langelandsvik, G.; Akselsen, O.; Furu, T.; Roven, H. Review of Aluminum Alloy Development for Wire Arc Additive Manufacturing. *Materials* **2021**, *14*, 5370. [CrossRef]
13. Kumar, N.; Bhavsar, H.; Mahesh, P.; Srivastava, A.; Bora, B.; Saxena, A.; Dixit, A. Wire Arc Additive Manufacturing—A revolutionary method in additive manufacturing. *Mater. Chem. Phys.* **2022**, *285*, 126144. [CrossRef]
14. Pickin, C.; Young, K. Evaluation of cold metal transfer (CMT) process for welding aluminum alloy. *Sci. Technol. Weld. Join.* **2013**, *11*, 583–585. [CrossRef]
15. Srinivasan, D.; Sevvel, P.; Solomon, I.; Tanushkumaar, P. A review on Cold Metal Transfer (CMT) technology of welding. *Mater. Today Proc.* **2022**, *64*, 108–115. [CrossRef]
16. Aldalur, E.; Suarez, A.; Veiga, F. Metal transfer modes for Wire Arc Additive Manufacturing AL-Mg alloys: Influence of heat input in microstructure and porosity. *J. Mater. Process. Technol.* **2021**, *297*, 117271. [CrossRef]
17. Schauerte, O. Titanium in automotive production. *Adv. Eng. Mater.* **2003**, *5*, 411–418. [CrossRef]
18. Stojanovic, B.; Bukvic, M.; Epler, I. Application of aluminum and aluminum alloys in engineering. *Appl. Eng. Lett. J. Eng. Appl. Sci.* **2018**, *3*, 52–62. [CrossRef]
19. Su, C.; Chen, X.; Konovalov, S.; Singh, R.; Jayalakshmi, S.; Huang, L. Effect of Deposition Strategies on the Microstructure and Tensile Properties of Wire Arc Additive Manufactured Al-5Si Alloys. *J. Mater. Eng. Perform.* **2021**, *30*, 2136–2146. [CrossRef]
20. Chakkravarthy, V.; Jerome, S. Fabrication of preferentially oriented Al4043 alloy and its wear anisotropy. *Mater. Lett.* **2020**, *280*, 128578. [CrossRef]
21. Liu, Z.; Zhang, P.; Li, S.; Wu, D.; Yu, Z. Wire and arc additive manufacturing of 4043 Al alloy using a cold metal transfer method. *Int. J. Miner. Metall. Mater.* **2020**, *27*, 783–791. [CrossRef]
22. Pramod, R.; Kumar, S.; Girinath, B.; Kannan, A.; Kumar, N.; Shanmugam, N. Fabrication, characterization, and finite element analysis of cold metal transfer-based wire and arc additive-manufactured aluminum alloy 4043 cylinder. *Weld. World* **2020**, *64*, 1905–1919. [CrossRef]
23. Vishnukumar, M.; Pramod, R.; Kannan, A. Wire arc additive manufacturing for repairing aluminum structures in marine applications. *Mater. Lett.* **2021**, *299*, 130112. [CrossRef]
24. Kotlarski, G.; Ormanova, M.; Ossenbrink, R.; Nikitin, A.; Doynov, N.; Valkov, S.; Michailov, V. Fabrication and Characterization of Wire Arc Additively Manufactured AlSi5 Structures. *Metals* **2022**, *12*, 1870. [CrossRef]
25. *ISO 6507-1:2018*; Metallic Materials—Vickers Hardness Test—Part 1: Test Method. ISO: Geneva, Switzerland, 2018.
26. *ISO 6892-1:2009*; MetallicMaterials—Tensile Testing—Part 1: Method of Test at Room Temperature. ISO: Geneva, Switzerland, 2009.
27. Saad, G.; Fayek, S.; Fawzy, A.; Soliman, H.; Mihammed, G. Deformation characteristics of Al-4043 alloy. *Mater. Sci. Eng. A* **2010**, *527*, 904–910. [CrossRef]
28. Vashista, M.; Paul, S. Correlation between full width at half maximum (FWHM) of XRD peak with residual stress on ground surfaces. *Philos. Mag.* **2012**, *92*, 4194–4204. [CrossRef]
29. Cullity, B. *Elements of X-ray Diffraction*, 2nd ed.; Cohen, M., Ed.; Addison-Wesley Publishing Company Inc.: Quezon, Phillippines, 1978.
30. Nakashima, P. The Crystallography of Aluminum and Its Alloys. In *Encyclopedia of Aluminum and Its Alloys*; Totten, G., Tiryakiolu, M., Kessler, O., Eds.; CRC Press: Boca Raton, FL, USA, 2018; pp. 488–586.
31. Köhler, M.; Hensel, J.; Dilger, K. Effects of Thermal Cycling on Wire and Arc Additive Manufacturing of Al-5356 Components. *Metals* **2020**, *10*, 952. [CrossRef]
32. Anyalebechi, P. Hydrogen Solubility in Liquid and Solid Pure Aluminum—Critical review of Measurement Methodologies and Reported Values. *Mater. Sci. Appl.* **2022**, *13*, 158–212. [CrossRef]
33. Rosso, E.; Santos, C.; Garcia, A. Microstructure, Hardness, Tensile Strength, and Sliding Wear of Hypoeutectic Al-Si Alloys with Small Cr Additions and Fe-Impurity Content. *Adv. Eng. Mater.* **2021**, *24*, 2001552. [CrossRef]
34. Batahgy, A. Effect of laser welding parameters on fusion zone shape and solidification structure of austenitic steels. *Mater. Lett.* **1997**, *32*, 155–163. [CrossRef]
35. Petrov, P.; Tongov, M. Numerical modelling of heat source during electron beam welding. *Vacuum* **2020**, *171*, 108991. [CrossRef]
36. Zhang, Y.; Zheng, K.; Liu, Y.; Shi, L.; Zhao, Q.; Tian, X. Efficient use of iron impurity in Al-Si alloys. *J. Alloys Compd.* **2014**, *615*, 594–597. [CrossRef]
37. Sinha, A.; Pramanik, S.; Yagati, K. Research progress in arc based additive manufacturing of aluminum alloys—A review. *Measurement* **2022**, *200*, 111672. [CrossRef]

38. Nikanorov, P.; Volkov, M.; Gurin, V.; Burenkov, Y.; Derkachenko, L.; Kardashev, B.; Regel, L.; Wilcox, W. Structural and mechanical properties of Al-Si alloys obtained by fast cooling of a levitated melt. *Mater. Sci. Eng. A* **2005**, *390*, 63–69. [CrossRef]
39. Derekar, K.; Addison, A.; Joshi, S.; Zhang, X.; Lawrence, J.; Xu, L.; Melton, G.; Griddiths, D. Effect of pulsed metal inert gas (pulsed-MIG) and cold metal transfer (CMT) techniques on hydrogen dissolution in wire arc additive manufacturing (WAAM) of aluminum. *Int. J. Adv. Manuf. Technol.* **2020**, *107*, 311–331. [CrossRef]
40. Wang, J.; Shen, Q.; Kong, X.; Chen, X. Arc Additively Manufactured 5356 Aluminum Alloy with Cable-Type Welding Wire: Microstructure and Mechanical Properties. *J. Mater. Eng. Perform.* **2021**, *30*, 7472–7478. [CrossRef]
41. Salazr-Guapuriche, M.; Zhao, Y.; Pitman, A.; Greene, A. Correlation of Strength with Hardness and Electrical Conductivity for Aluminum Alloy 7010. *Mater. Sci. Forum* **2006**, *519*, 853–858.
42. Wieczorowski, M.; Pereira, A.; Carou, D.; Gapinski, B.; Ramirez, I. Characterization of 5356 Aluminum Walls Produced by Wire Arc Additive Manufacturing (WAAM). *Materials* **2023**, *16*, 2570. [CrossRef]

Disclaimer/Publisher's Note: The statements, opinions and data contained in all publications are solely those of the individual author(s) and contributor(s) and not of MDPI and/or the editor(s). MDPI and/or the editor(s) disclaim responsibility for any injury to people or property resulting from any ideas, methods, instructions or products referred to in the content.